

JGR Space Physics

RESEARCH ARTICLE

10.1029/2021JA029804

Special Section:

Probing the Magnetosphere through Magnetoseismology and Ultra-Low-Frequency Waves

Key Points:

- MHD modeling shows FLRs outside the plasmasphere move earthward from the initial to main phase of geomagnetic storms
- Caused by (a) decreased field line eigenfrequencies due to enhanced plasma densities and weaker magnetic fields
- (b) Higher fast waveguide frequencies, due to changes in density/boundary locations, which drive the FLRs

Correspondence to:







T. Elsdén,
thomas.elsden@glasgow.ac.uk

Citation:

Elsden, T., Yeoman, T. K., Wharton, S. J., Rae, I. J., Sandhu, J. K., Walach, M.-T., et al. (2022). Modeling the varying location of field line resonances during geomagnetic storms. *Journal of Geophysical Research: Space Physics*, 127, e2021JA029804. <https://doi.org/10.1029/2021JA029804>

Received 16 JUL 2021
Accepted 21 DEC 2021

Modeling the Varying Location of Field Line Resonances During Geomagnetic Storms

T. Elsdén^{1,2} , T. K. Yeoman² , S. J. Wharton^{2,3}, I. J. Rae⁴ , J. K. Sandhu⁴ , M.-T. Walach⁵ , M. K. James² , and D. M. Wright²

¹School of Mathematics and Statistics, University of Glasgow, Glasgow, UK, ²School of Physics and Astronomy, University of Leicester, Leicester, UK, ³Researchers in Schools, London, UK, ⁴Department of Mathematics, Physics and Electrical Engineering, Northumbria University, Newcastle, UK, ⁵Physics Department, Lancaster University, Lancaster, UK

Abstract Previous observational studies have shown that the natural Alfvén frequencies of geomagnetic field lines vary significantly over the course of a geomagnetic storm, decreasing by up to 50% from their quiet time values outside the plasmasphere. This was recently demonstrated statistically using ground magnetometer observations across 132 geomagnetic storm events (Wharton et al., 2020). This then brings into question where field line resonances (FLRs) will form in storm-time conditions relative to quiet times. With storm-time radiation belt dynamics depending heavily upon wave-particle interactions, understanding how FLR locations change over the course of a storm will have important implications for this area. Using 3D magnetohydrodynamic (MHD) simulations, we investigate how changes in the Alfvén frequency continuum of the Earth's dayside magnetosphere over the course of a geomagnetic storm affect the fast-Alfvén wave coupling. By setting the model Alfvén frequencies consistent with the observations, and permitting a modest change in the plasmopause/magnetopause locations consistent with storm-time behavior, we show that FLR locations can change substantially during storms. The combined effects of higher fast waveguide frequencies and lower Alfvén frequencies during storm main phases, act together to move the FLR locations radially inwards compared to quiet times. FLRs outside of the plasmasphere are moved radially inward by 1.7 Earth radii for the cases considered.

Plain Language Summary Geomagnetic storms are the most energetic events in our Earth's near space environment, causing huge morphological changes over timescales from a few hours to several days. This study considers how such changes affect the propagation of low frequency electromagnetic waves in the space around the Earth dominated by Earth's magnetic field (the magnetosphere). It is important to understand how these waves may vary during geomagnetic storms, due to their interaction with energetic particles which can be hazardous to orbiting spacecraft. Furthermore, from a general physics standpoint, it is of interest to understand how energy is transported throughout the system by such waves. Overall we find that, between the initial and main phases of a storm, there are significant changes in the locations where a particular class of low frequency waves will manifest. The simple broad conclusion from this paper is that storms change the morphology of Earth's magnetosphere, which then significantly changes the properties of the waves in the system.

1. Introduction

Ultra-low frequency (ULF; ~ 1 mHz-1 Hz) waves (Jacobs et al., 1964) play a central role in magnetospheric dynamics, affecting, for example, radiation belt particles (Claudepierre et al., 2013; Degeling et al., 2007; El-kington et al., 1999, 2003; Foster et al., 2015; Hao et al., 2019; Mann et al., 2013; Q. G. Zong et al., 2009), field-aligned currents (Milan et al., 2001; Rankin et al., 2005), and energization/de-energization of the ring current (Li et al., 2021; Liu et al., 2020; Murphy et al., 2014; Oimatsu et al., 2018; Yang et al., 2011). The temporal and spatial variation of these low frequency waves are dependent on many factors, however can be primarily summarized as varying with the driver (solar wind conditions) and magnetospheric structure (magnetic field configuration, plasma density, location of magnetopause/plasmopause). Given that during geomagnetic storms all of these features are highly dynamic, it is of little surprise that storm-time ULF waves also vary substantially, which is the topic of this study. This introduction will first offer a brief summary of the important ULF wave theory to appreciate the research in question, followed by highlighting relevant observations of ULF waves during storms, before outlining the proposed objectives of this study.

1.1. ULF Wave Theory

The cold plasma of the dayside outer magnetosphere supports two fundamental low frequency modes of oscillation, which can be described by the framework of magnetohydrodynamics (MHD). First there exists the fast MHD wave, which propagates in all directions and compresses/rarefies the plasma (Dungey, 1955; Herlofson, 1950). Second is the Alfvén wave, a transverse wave which propagates strictly along the background field (Alfvén, 1942; Dungey, 1955). In the magnetosphere, the fast modes can manifest as cavity (Kivelson & Southwood, 1986) or waveguide (Samson et al., 1992) modes, whereby fast waves propagate between boundaries in the magnetosphere (e.g., plasmopause/magnetopause or turning point) to form radially standing modes. Beyond the turning point, these radially standing waves have an evanescent radial structure. The difference between the cavity and waveguide nomenclature arises from considering a closed magnetosphere (cavity), which only permits a discrete azimuthal normal mode structuring, or an open ended magnetosphere (waveguide, i.e., with flow into the magnetotail), which allows for a continuous spectrum of azimuthal wavenumbers (Southwood, 1968, 1974; Mann et al., 1999).

Alfvén waves manifest most prominently in the magnetosphere as field line resonances (FLRs; Chen & Hasegawa, 1974; Southwood, 1974). These are Alfvén waves standing along geomagnetic field lines that have been driven at their natural frequency by a fast mode as described above. The Alfvén frequency of a field line depends upon the length of the field line, the magnetic field strength and structure, the plasma density along the field line and the wave polarisation (Radoski, 1967; Singer et al., 1981). At the radial location where the global fast mode frequency matches the local Alfvén frequency, the modes couple, with energy being transferred from the fast to Alfvén wave, resulting in a resonant growth of the Alfvénic perturbation (Allan et al., 1986, 1985; Inhester, 1987; D.-H. Lee & Lysak, 1989; Kivelson & Southwood, 1985; Kivelson & Southwood, 1986; Wright, 1994). These waves have a rich history in theory and observation, being invoked as the explanation for a myriad of ULF wave observations both on the ground (e.g., Samson et al., 1971) and in space (e.g., Hartinger et al., 2011; Rae et al., 2005).

ULF waves have many sources, typically classified by the origin of the driver being external or internal to the magnetosphere. Externally, broadband fluctuations in the solar wind dynamic pressure drive significant ULF wave activity, either by continuous buffeting of the magnetopause or step-like pressure changes associated with interplanetary shocks (e.g., Chi et al., 2006; Takahashi & Ukhorskiy, 2007). The often Kelvin-Helmholtz unstable flank magnetopause can further be a source of fast waves, exciting surface modes of the magnetopause with a radially evanescent structure (Southwood, 1968, 1974). Enhanced flow speeds in the flank magnetosheath can also lead to the efficient excitation of waveguide modes (Mann et al., 1999). More recently, transient phenomena originating from the foreshock have been shown to drive a plethora of ULF waves [Shen et al., 2018; Wang et al., 2018, 2021; see also Section 2.3 of the review by Q. Zong et al. (2017) and references therein]. Internal driving mechanisms usually involve wave-particle interactions, whereby energetic particles resonantly interact with ULF waves, most notably through the drift and drift-bounce resonance mechanisms (Southwood et al., 1969; Southwood & Kivelson, 1981, 1982).

1.2. ULF Waves During Geomagnetic Storms

Geomagnetic storms represent an energization of the entire magnetospheric system, caused by long periods of strong solar wind driving, in particular when a southward interplanetary magnetic field (IMF) permits efficient reconnection at the dayside magnetopause (Akasofu et al., 1963; Dungey, 1961; Gonzalez et al., 1994). Storms usually contain three distinct phases: initial, main, and recovery (e.g., Hutchinson et al., 2011), which can be tracked by the effect of the enhanced storm time ring current on the low latitude magnetic field strength, through the Dst or Sym-H indices (e.g., Iyemori, 1990). In the initial phase, increased solar wind dynamic pressure compresses the dayside magnetosphere. When the rate of dayside reconnection is high, this triggers the main phase, inputting vast amounts of energy into the magnetosphere (Kozyra et al., 1998). This is accompanied by an enhancement of the ring current, which is tracked by a dramatic decrease in Sym-H, due to the depression of the low latitude magnetic field strength. The system then slowly returns to pre-storm conditions in the recovery phase, marked by an increasing Sym-H. The timescales for each phase are highly variable, dependent on the storm driving mechanism and strength of the storm [as noted by e.g., Murphy et al. (2018)]. However, as an average for moderate conditions, Hutchinson et al. (2011) found durations of ~6, ~9, and ~54 hr for the initial, main and recovery phases.

Over the duration of a storm, the Alfvén eigenfrequencies for dayside field lines outside the plasmasphere have been shown to decrease significantly. This has been noted by many authors using empirical magnetic field and density models parameterized by Dst index (Sandhu et al., 2017; Wild et al., 2005), and statistically using 10 years of IMAGE ground magnetometer data binned by Sym-H index (Wharton, Wright, Yeoman, James, et al., 2019; Wharton, Wright, Yeoman, & Reimer, 2019). Furthermore on a case study basis, investigating the Halloween storm of October 2003, several authors reported such decreases in the eigenfrequencies (Chi et al., 2005; Kale et al., 2009; Takasaki et al., 2006). Similar trends in the eigenfrequencies have been recorded for other events (e.g., Takahashi et al., 2002; E. A. Lee et al., 2007; Rae et al., 2019).

Changes in the eigenfrequencies must be caused by changes in the magnetic field strength/structure and/or the plasma mass density. This opens a complex discussion on the various importance of these competing effects, which have significant temporal and spatial dependence during storms. For example, Rae et al. (2019) found that the enhanced storm time ring current caused significant enough depressions in the magnetic field strength to decrease the eigenfrequencies outside of $L = 3.4$. Sandhu et al. (2018) considered how the eigenfrequencies of the outer magnetosphere ($5.9 < L < 9.5$) vary for low Dst index. Sandhu et al. (2018) found that despite their empirical density model (Sandhu et al., 2017) showing a decrease in plasma mass density (which would increase frequencies), the eigenfrequencies decreased due to a decrease in the magnetic field strength. This is aided by the fact that the Alfvén speed varies proportional to the magnetic field strength, but only the square root of the density (e.g., Corpo et al., 2019; Dent et al., 2006; Menk et al., 2014; Takahashi et al., 2002; Takahashi et al., 2006). Storm time cold plasma dynamics, in particular the influence of heavy ions on the radial mass density (and hence Alfvén velocity/frequency) profile, have been the focus of many studies. Fraser et al. (2005) showed that the presence of heavy ions, in particular the formation of the oxygen torus (Gkioulidou et al., 2019; Roberts et al., 1987) outside of the storm-time contracted plasmopause can lead to a significant increase in the mass density. Similar results are also shown by Menk et al. (2014). Furthermore, ULF waves have been shown to interact with and modulate the outflow of dayside ionospheric heavy ions such as O^+ (Liu et al., 2019). The picture is further complicated by the fact that the refilling of the plasmasphere after heightened periods of geomagnetic activity is by no means a steady process, and indeed has significant local time variation (Dent et al., 2006). As such it should be highlighted that in this study, we will be considering the behavior of FLRs in the plasmatrough, removing the difficulty of accounting for the substantial variability of the near plasmopause storm time dynamics.

1.3. Study of Wharton et al., 2020

To understand the behavior of the Alfvén eigenfrequencies during storm intervals, rather than simply during intervals parameterized through Dst, Wharton et al. (2020) studied a catalog of 132 storms (Walach & Grocott, 2019) in order to separate out the competing effects of varying magnetic field strengths and plasma mass densities. Using a cross-phase analysis (Baranskii et al., 1985; Waters et al., 1991; Wharton et al., 2018) of ground magnetometer observations, together with a superposed multiple-epoch method for comparison of each storm (Hutchinson et al., 2011), the eigenfrequency variation with L-shell (over $3.15 \leq L \leq 6.42$) and MLT for each phase of a geomagnetic storm was analyzed. When combined with an empirical field model (Tsyganenko & Sitnov, 2005), this frequency variation could be used to infer the plasma mass density by solving the Alfvén wave equation (Singer et al., 1981). Through such analysis, the authors concluded that the fundamental Alfvén frequency decreased across all dayside MLT sectors for $L > 4$ during storm main phase. This was caused by a weakening of the magnetic field strength together with an increased plasma mass density. The trend for $L < 4$ was substantially different, with an overall increase in the eigenfrequency from initial to main phase. This was attributed to a decrease in the plasma mass density at a given L , based on plasmaspheric erosion, such that a field line originally within the plasmasphere lie outside by the main phase. Again, we emphasize that the results in the present study will be based on the plasmatrough eigenfrequency profiles, on average outside of $L = 4$ for the storm catalog of Wharton et al. (2020).

1.4. Goals of This Study

This paper is based on modeling the observations of Wharton et al. (2020) to understand how the changing Alfvén continuum over the course of a geomagnetic storm affects the fast-Alfvén wave coupling of the dayside magnetosphere. In particular, we test the hypothesis that during geomagnetic storms, outside of the plasmasphere FLRs form further Earthward. To this end, we will consider comparative MHD simulations of the initial and

main phase equilibria to examine where FLRs form in each case. This will involve a detailed study of the fast waveguide modes responsible for driving the FLRs. Furthermore, we will analyze the effect of boundary motion (plasmopause/magnetopause) over the course of a storm on the wave coupling.

The paper is structured as follows: Section 2 introduces the observations of Wharton et al. (2020), expanding upon the analysis in that paper to provide the variation of Alfvén eigenfrequencies with L-shell and MLT over the course of a geomagnetic storm. Section 3 explains the numerical model used for the simulations, with results presented in Section 4. Discussion and conclusions follow in Sections 5 and 6 respectively.

2. Observations

The modeling work presented here was motivated by the observational study of Wharton et al. (2020), and a brief summary of the data analysis employed there is given below. Wharton et al. (2020) used the north–south component of 10-s resolution magnetometer data from the International Monitor for Auroral and Geomagnetic Effects (IMAGE) array (Lühr, 1994) to investigate how the eigenfrequencies of magnetic field lines changed during geomagnetic storms. The eigenfrequencies were determined using the cross-phase technique of Waters et al. (1991), which requires two latitudinally and closely spaced ground-based magnetometers. Two are required to detect the phase change with latitude that occurs at the resonant frequency of the midpoint of the magnetometers. Several papers have automated this technique (e.g., Wharton et al., 2018; Wharton, Wright, Yeoman, James, et al., 2019; Wharton, Wright, Yeoman, & Reimer, 2019). Wharton et al. (2020) employed six such magnetometer pairs covering a range of L shells from 3.15 to 6.42. The phase changes were calculated using a Lomb-Scargle (LS) cross-phase technique previously employed by Wharton, Wright, Yeoman, James, et al., 2019; Wharton, Wright, Yeoman, & Reimer, 2019 that could process unevenly spaced data and use a higher frequency resolution because the frequency grid is independent of the properties of the data used. The chosen frequency resolution was 4 times that achievable with a discrete Fourier transform. The dynamic cross-phase spectrum uses a 40-min sliding window and provides a frequency resolution of 0.104 mHz.

The superposed multiple-epoch analysis method used by Hutchinson et al. (2011) was then applied to the derived cross-phase spectra. This method treats the three phases of geomagnetic storms separately by calculating the mean duration of each of the three storm phases (initial, main, and recovery). A superposed epoch analysis was then applied to each storm phase, elongating or contracting each phase in time as appropriate. This created a common time grid to which the three phases of each storm were normalized to in order to observe the general trends in each of the three storm phases, independent of their duration.

These techniques were applied to a set of storm intervals between 2002 and 2018 (in order to examine at least one solar cycle of observations) characterized using the method described in Walach and Grocott (2019) to identify the start and end time of the storm initial, main, and recovery phases. This process yielded a list of 132 storm intervals for analysis.

Wharton et al. (2020) extracted the fundamental eigenfrequency of the geomagnetic field lines from the cross-phase measurements, following the techniques used by Berube et al. (2003) and Wharton et al. (2018). The plasma mass density implied by the eigenfrequency measurement was then determined by solving the MHD wave equation of Singer et al. (1981). The magnetic field in this solution was represented by the model of Tsyganenko and Sitnov (2005), parameterized by Sym-H index, solar wind dynamic pressure and velocity, IMF y and z components, and the dipole tilt angle. These values were calculated using an identical superposed multiple-epoch analysis method as applied to the cross phase measurements. The distribution of plasma mass density along the field line was assumed to be a power law of r^{-3} (e.g., Menk et al., 1999), where r is the radial position along the field line, with the plasma mass density then characterized by the inferred equatorial density.

In Wharton et al. (2020), the process of estimating the equatorial mass density described above was repeated for each of the six station pairs for three MLT sectors, 6–10, 10–14, and 14–18 MLT, providing a radial profile of equatorial plasma mass density in three local time sectors (Figure 8 of Wharton et al., 2020). Figure 1 shows radial profiles of the Alfvén eigenfrequencies corresponding to these plasma mass densities. The bottom panel shows the superposed multiple-epoch analysis of the Sym-H data taken from Wharton et al. (2020). In this panel, the dashed black line shows the mean Sym-H value from the superposed epoch calculation, with the yellow solid

Alfvén Eigenfrequency Continua

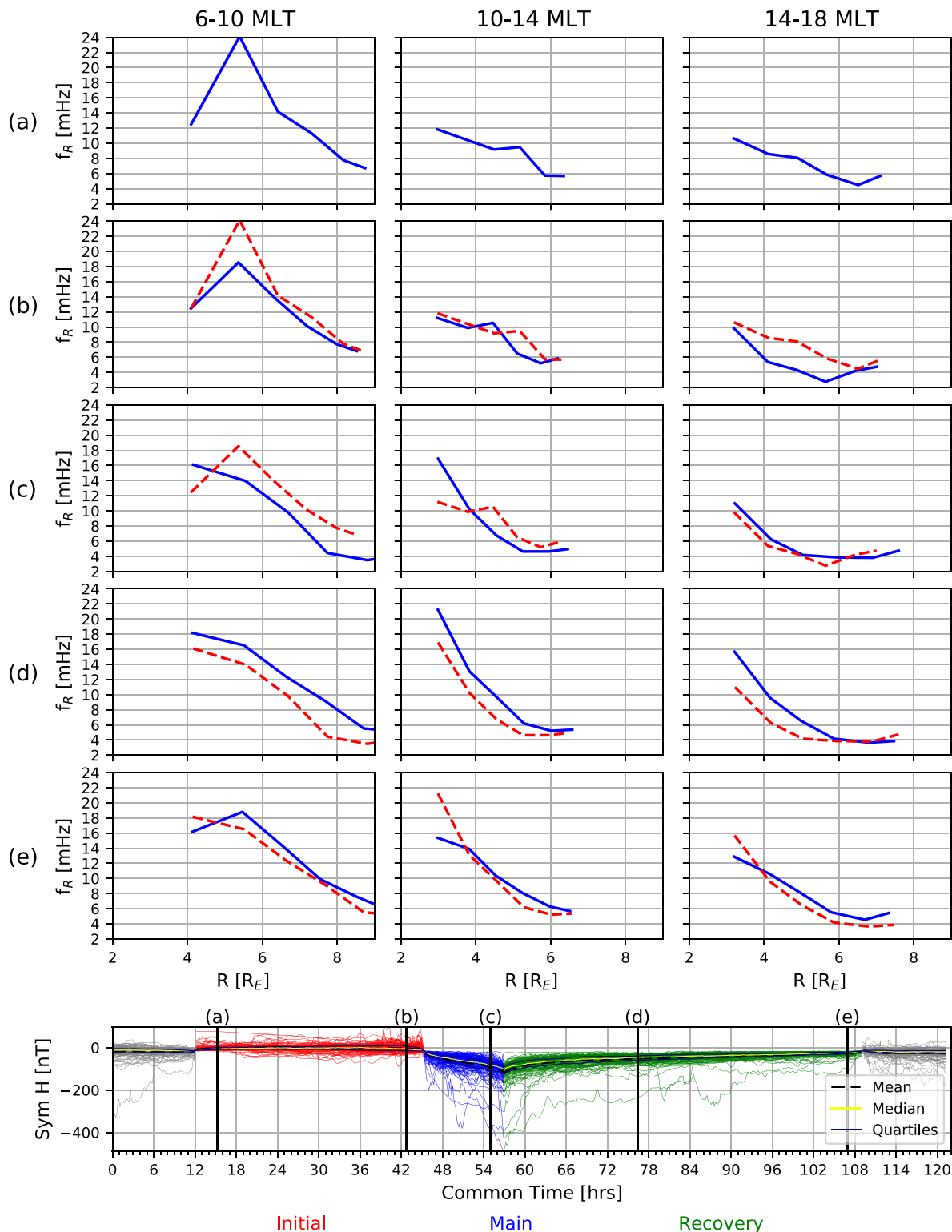


Figure 1.

line, showing the corresponding median value, and the solid blue lines, showing the upper and lower quartiles. The Sym-H values associated with the individual storm events are also included, with the initial phase shown in red, the main phase in blue, and the recovery phase in green. The upper panels show the radial profiles of the median Alfvén eigenfrequency at different phases of a geomagnetic storm. Each column represents data from the 6–10, 10–14, and 14–18 MLT sectors from left to right. Each row shows the magnetospheric state at five intervals during the average geomagnetic storm, marked (a) to (e) on the Sym-H index plot at the bottom. Blue solid lines show the eigenfrequencies at that interval of the storm, and red dashed lines show the previous interval for comparison. Comparing the MLT columns in Figure 1, a significant local time asymmetry in the eigenfrequency profiles is apparent throughout storms, with higher eigenfrequencies observed on the dawn side compared to the dusk side. Comparing the storm-phase rows in Figure 1 reveals that for all MLT sectors, the eigenfrequency profiles decrease in value from Figures 1a–1c and then increase again from Figures 1c–1e. The main phase of the storms is characterized by a minimum in eigenfrequency at all local times. The variation in eigenfrequency profile in the 6–10 MLT sector (left hand column) between the initial phase of the storm (row a) and the main phase of the storm (row c) will form the focus of the modeling study described below (the reasons for which are given at the beginning of Section 4).

3. 3D Numerical Dipole MHD Model

3.1. Model Details

In this study, we utilize the linear, MHD numerical model described fully by Wright and Elsden (2020), with only the key properties discussed here. This model solves the linear, low- β , resistive MHD equations in a background 3D dipole magnetic field. It uses a field-aligned orthogonal coordinate system (α, β, γ), where α labels L-shells, β is the azimuthal direction, and γ is the field-aligned direction. The computational grid spacing is optimized to allow for more uniform coverage along a field line as often plagues models using dipole coordinate systems (Kageyama et al., 2006). This actually enables fewer points to be required along a field line and permits unprecedented resolution perpendicular to the field. This is a very desirable quality for studying FLRs, where small scales develop perpendicular to field lines through phase mixing (Mann et al., 1995). Indeed, such FLR resolution is a key requirement for this study, which could not be achieved with other global magnetospheric MHD codes. For example, the simulations performed in this study have a radial resolution in the equatorial plane of $0.05 R_E$ at all L-shells.

The magnetopause acts as the simulation outer boundary and can be set to any location, that is, it does not need to coincide with a coordinate surface. Therefore, we use the Shue magnetopause model (Shue et al., 1997) to define this boundary. The inner boundary would usually be indicative of the plasmopause location. This boundary is simply perfectly reflecting and can be placed at any L-shell. The upper ends of the field lines are modeled also with a perfectly reflecting condition, indicative of a perfectly conducting ionosphere. The location of the upper boundaries can be varied to any point along a particular reference field line (see Figure 1d of Wright and Elsden, 2020). We solve only over the northern hemisphere, with a symmetry condition present at the equator, which halves the simulation domain for numerical efficiency. The simulations assume an antinode of the velocity at the equator (node of perpendicular magnetic field), which yields only the odd field-aligned harmonics. We could choose to include even harmonics as well, though this would require the solution over both hemispheres and would not impact the overall conclusions from this study.

Dissipation is included throughout the domain in the form of resistivity, which will act to limit the scale length that FLRs will phase-mix down to, allowing the smallest scales appearing to be adequately resolved. The details of the form of the resistivity and numerical considerations for this are provided in Section 3.4 of Wright and Elsden (2020). Given the axisymmetric dipole field which does not well represent the distorted tail field, the model is not suited for studying nightside phenomena. Therefore, we simulate propagation and loss to the tail

Figure 1. Variation in Alfvén eigenfrequencies corresponding to plasma densities calculate by Wharton et al. (2020). The bottom panel shows the superposed multiple-epoch analysis of the Sym-H data from Wharton et al. (2020). The dashed black line shows the mean Sym-H value, the solid yellow line shows the median, and the solid blue lines show the upper and lower quartiles, with the initial phase individual Sym-H values shown in red, the main phase in blue, and the recovery phase in green. The upper panels show the median radial Alfvén eigenfrequency profiles at different phases of a geomagnetic storm. Each column represents data from the 6–10, 10–14, and 14–18 MLT sectors from left to right. Each row shows the magnetospheric state at five intervals during the average geomagnetic storm, marked on the Sym-H index plot at the bottom. Blue solid lines show the eigenfrequencies at that interval of the storm, and red dashed lines show the previous interval for comparison.

by introducing a dissipative region beyond a certain X value (here, we use $X = -6 R_E$, where X is the Earth-Sun line). In this region, a linear drag term is added to the equation of motion which acts to reduce wave amplitudes before reaching the true far simulation boundary, such that they never return to the solution region of interest. The use of such a model is further justified in the current study by only having eigenfrequency data from the study of Wharton et al. (2020) for the dayside magnetosphere.

The code has been thoroughly tested, with energy conservation satisfied to one part in 10^4 for a typical run. The timestep is uniform across the simulation and is chosen to satisfy the minimum of that required by the Courant–Friedrichs–Lewy (CFL) condition (de Moura & Kubrusly, 2013) and the diffusive timescale imposed by resistivity. The simulation is run in dimensionless units and as such an appropriate normalization is required to make the results meaningful. All results will be presented here in physical units; however, the normalizing values used are listed for completeness and replicability of the results. Values are normalised by: magnetic field strength $B_0 = 200$ nT; length $L_0 = 1R_E = 6371$ km; time $T_0 = 7.543$ s; velocity $V_0 = 844.62$ kms⁻¹; frequency 132.568 mHz; density $\rho_0 = 26.871$ amu cm⁻³; and current density $j_0 = 0.02498$ μ Am⁻². The values of other model parameters, again listed to aid with the future reproduction of results are: grid size in (α, β, γ) of $300 \times 450 \times 50$; grid spacing along the field uses $s_l = 8.0$, $s_u = 12.0$, $\sigma = 3.0$, $r_g = 11.5$ (see Wright and Elsden (2020); Equations 20 and 21 for full details of these terms); resistivity $\eta = 0.001$.

3.2. Model Setup—Inputting Observed Frequencies

To model the observed ULF waves during storms, the key parameter to be fixed is the observed wave frequency. Given that the model has a fixed background magnetic field structure, the frequency is varied on a particular field line by changing the density. We can therefore input the observed radial frequency profiles at a particular MLT into the model in the following way:

1. Fit a smooth, continuous function to the observed frequencies in Figure 1, $f_A(L)_{\text{obs}}$
2. Calculate the model Alfvén eigenfrequencies as a function of L-shell, for the desired model geometry (i.e., field line lengths). We choose a density variation along the field according to

$$\rho = \rho_{eq} \left(\frac{r_{eq}}{r} \right)^4, \quad (1)$$

and the equatorial Alfvén speed is set to 1 (in normalised units). The Alfvén frequencies are calculated by solving the undriven Alfvén wave equation of Singer et al. (1981) for the 3D dipole geometry. The Alfvén wave polarisation is assumed to be toroidal, consistent with the observational analysis of the North-South ground magnetic field component. This yields the model Alfvén frequency $f_A(L)_{\text{model}}$, as a function of L-shell.

3. The model Alfvén speed can now be adjusted such that the model frequencies match the observed frequencies, by setting $V_A(L)_{\text{model}} = f_A(L)_{\text{obs}} / f_A(L)_{\text{model}}$, together with the appropriate normalization. This can perhaps more easily be pictured as first setting the Alfvén speed as $V_A(L) = 1/f_A(L)_{\text{model}}$ to “flatten” the model frequencies, such that the frequency is constant in L . This is then multiplied by the observed frequency profile, $f_A(L)_{\text{obs}}$

The method outlined above has been previously used to successfully input observed frequencies into a similar MHD model (Wright et al., 2018). Setting the model frequencies in this way will by default imply that the model densities do not match exactly to observed densities, since we are assuming a dipole magnetic field structure. In areas where the field departs significantly from a dipole, this approximation will break down. However, by restricting our attention to the dayside magnetosphere where the field is approximately dipolar, the model densities should be within realistic values.

3.3. Model Testing—Monochromatic Driver

We first check that the frequencies have been inputted correctly into the model from the observations. We can do this by driving the system monochromatically and checking whether a FLR forms in the location corresponding to that frequency as per the observed frequency profile. When driven for long enough at one frequency, this driving frequency will dominate over any natural fast waveguide response. We use the profile in the first column (6–10 MLT), panel (a) of Figure 1 to test this, with no azimuthal asymmetry (i.e., the radial variation is the same for all local times).

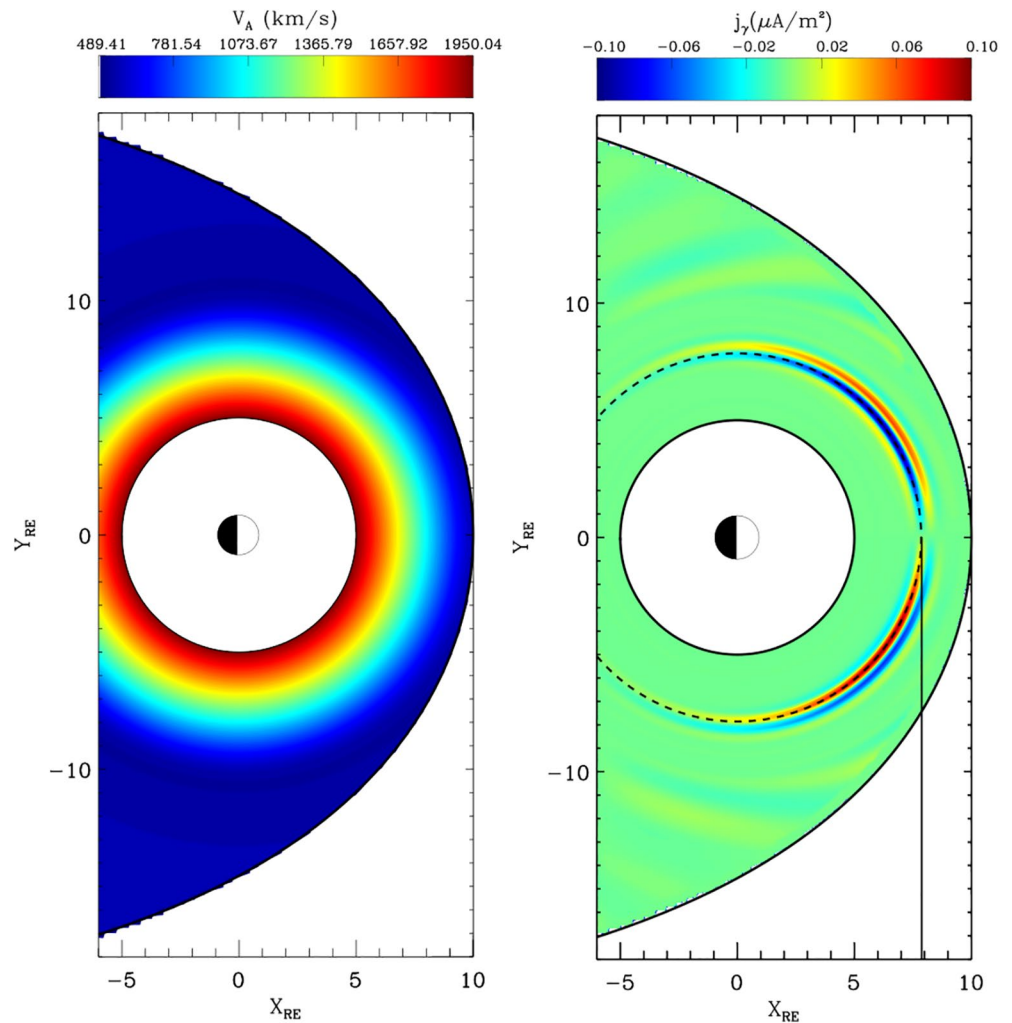


Figure 2. *Left:* Equilibrium Alfvén speed in the equatorial plane, which produces the observed Alfvén frequencies. *Right:* Field-aligned current j_γ from the end of the field lines mapped to the equatorial plane. Solid vertical black line at $\sim 8R_E$ represents the location of the expected field line resonance; dashed circle on this L-shell highlights model symmetry.

The left hand panel of Figure 2 displays the resulting equilibrium Alfvén speed in the equatorial plane to produce the observed frequencies. It should be noted that beyond $10R_E$ in the model (i.e., on the flanks), the Alfvén speed smoothly transitions to a constant value, but still varies along field lines through Equation 1. The right hand panel of Figure 2 displays the field-aligned current j_γ from near to the end of the field lines, mapped along field lines to the equatorial plane. This is done to present clearly the FLR locations; given that the field-aligned current is maximized at the end of the field lines where there is an antinode of the perpendicular magnetic field. The magnetopause has been driven monochromatically with perturbations to the compressional magnetic field component (b_γ) at 8 mHz, over an azimuthal extent of ~ 9 – 15 MLT, and the snapshot shown is taken after several driving periods. The clear amplitude peak in j_γ at $\sim 8R_E$ matches that expected from the frequency given in the top left panel of Figure 1.

The overall FLR structure has a node at noon, which is caused by using a driver symmetric about the noon meridian. Such symmetry results in a node of the azimuthal magnetic pressure gradient there, which is the quantity responsible for driving FLRs. The FLR extends in azimuth along a particular L-shell, around to the location where there is still significant enough power in the driver to elicit an FLR response. The right panel shows the field-aligned current density at a particular time, but over the course of one wave period there will be a radially outward phase motion across the resonance width. If aurorae were generated from such an FLR, they would be

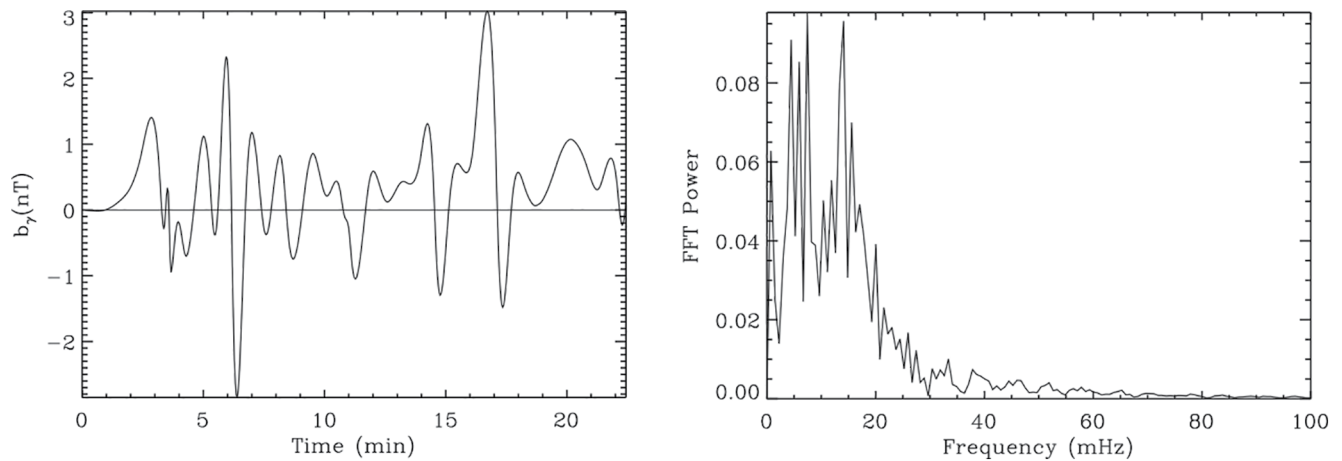


Figure 3. *Left:* Time series of field-aligned magnetic field component b_y applied on the magnetopause boundary to drive the simulation. *Right:* Fast Fourier transform (FFT) of driver time series on the left.

observed with a poleward phase motion of the auroral arcs (Milan et al., 2001; Rankin et al., 2005). This test simulation clearly shows that the observed frequency profile can be effectively placed into the model.

4. Modeling Results

In this initial study, we are not going to consider the azimuthal asymmetry as present in the observations. The key feature to capture is the reduction in the eigenfrequencies from the initial to main phase (i.e., column 1 panels (a) and (c) in the first column of Figure 1). The full azimuthal asymmetry will introduce considerable complexity in both the propagation characteristics of the fast modes (Wright et al., 2018) and polarisation properties of the FLRs (Elsden & Wright, 2017). As such, azimuthal asymmetry will be the subject of a follow-up study.

Furthermore, we must consider that the boundaries (i.e., plasmopause and magnetopause) will move significantly over the course of a storm. Therefore, we will present results from four simulations, with the plasmopause and subsolar magnetopause at $L = 4, 5 R_E$ and $L = 9, 10 R_E$ respectively for each of the profiles (a) and (c) in Figure 1. This is not meant to exactly represent the location of these boundaries for any particular storm. Indeed, the observations are averaged over 132 storms and hence include a variety of different boundary locations. We are merely trying to study the effect that moving the boundaries can have on the FLR locations. Staples et al. (2020) showed that on average, in response to a storm sudden commencement, the median subsolar magnetopause location varies from $10.7 R_E$ to $8.7 R_E$. The plasmopause model of O'Brien and Moldwin (2003) demonstrates that during storm times the plasmopause can occupy a wide range of locations with an average value of $L = 4$. These studies justify to a rough degree our chosen boundary locations, but it is emphasized that the following results would hold irrespective of the exact boundary locations used.

4.1. Simulation Driven Boundary Condition

Each of the four simulations presented in the following sections has been driven in the same way. On the magnetopause boundary, the field-aligned magnetic field component b_y is varied in time as shown in the left hand panel of Figure 3. This corresponds to magnetic pressure variations, consistent with the magnetopause response to the random buffeting by the solar wind dynamic pressure. The right hand panel of Figure 3 displays the fast Fourier transform (FFT) of the driver time series, showing that power is inputted over an approximate bandwidth of 0–20 mHz. The driver is symmetric about the noon meridian, covering an azimuthal extent of approximately 9–15 MLT. The variation of the driver along the field lines is such that there is an antinode of the compressional magnetic field at the equator, with a full width at half maximum (FWHM) of $6 R_E$. The key aspect of the driver regarding the results of this study is the frequency bandwidth, as this determines the effectiveness to which the waveguide mode harmonics can be excited. As long as this bandwidth encompasses the frequencies of the lower waveguide harmonics, our results will remain robust to the exact form of the driver. The spatial structure of the driver will affect the particular waveguide mode excited, as well as the resulting FLR azimuthal structure (Wright

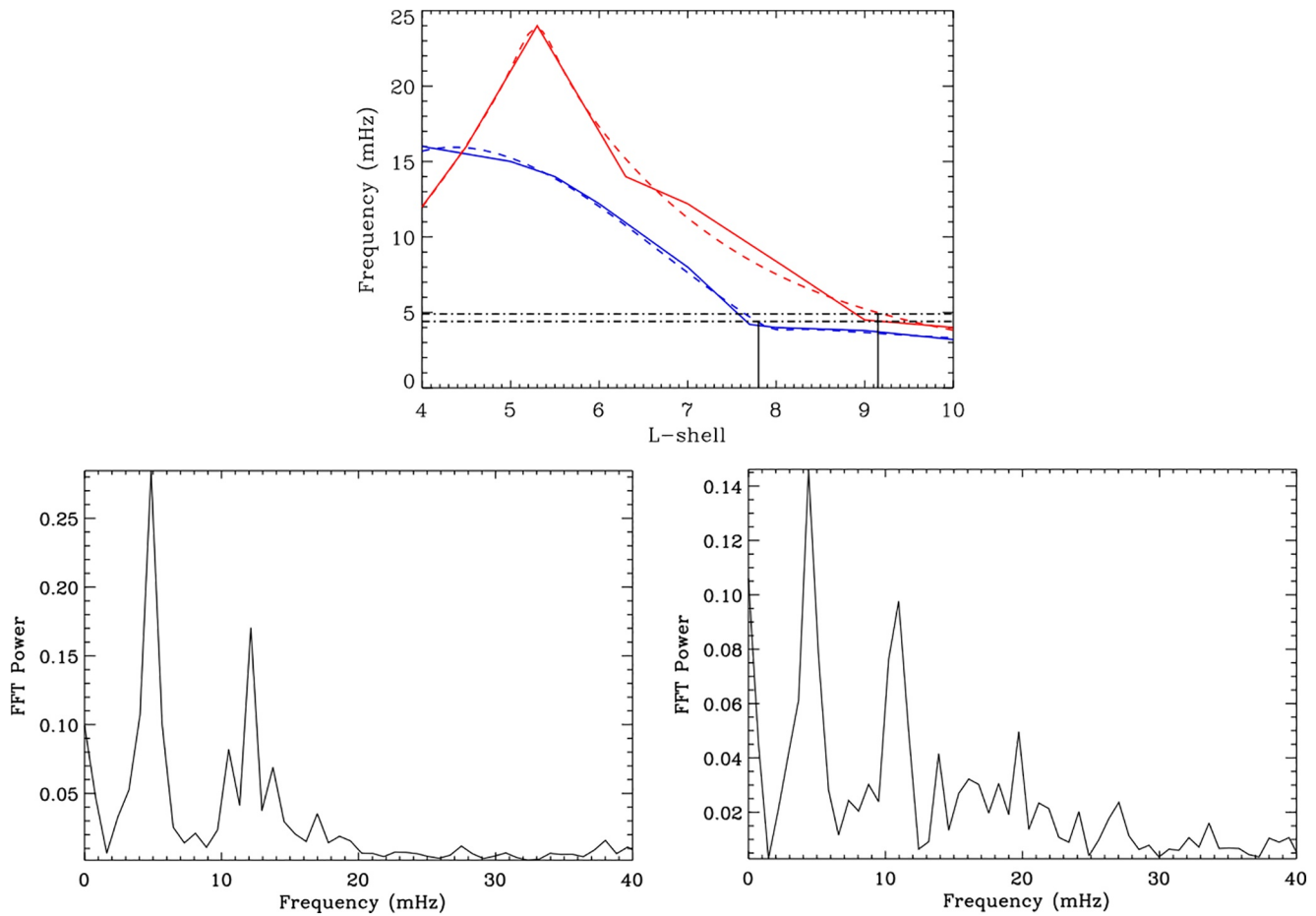


Figure 4. Top: Fits (dashed lines) to observed Alfvén frequency profiles (solid lines, from Figure 1) to be used in the model. Red lines are for the initial storm phase profile, blue for the main storm phase. Horizontal-dashed lines represent model fast waveguide frequencies, with vertical solid lines showing where the expected FLRs will form. Bottom left: Fast Fourier transform (FFT) showing fast waveguide frequencies for initial phase simulation. Bottom right: FFT displaying fast waveguide frequencies for main phase simulation. Simulation boundaries at noon are at $L = 5 R_E$ and $L = 10 R_E$.

& Elsdén, 2020). However, the overall trend of the radial location of FLR formation presented in this study would not be affected by asymmetries in the driver.

4.2. Simulation With a $5 R_E$ Plasmapause and a $10 R_E$ Magnetopause

To set up the simulations, we fit smooth, continuous functions to the observed frequency profiles in column 1, rows (a) and (c) of Figure 1. The observed profiles are shown as the colored solid lines in the top panel of Figure 4, with the fits shown as the colored dashed lines. The red lines represent initial storm phase profiles, and the blue lines represent the main phase profiles. The frequency fits have been extended out to $10 R_E$ for inputting into the model, beyond where the ground-based observations of Figure 1 provide measurements, in a consistent fashion.

We first consider the case where the plasmapause is placed at $L = 5 R_E$ and the subsolar magnetopause at $L = 10 R_E$. The magnetopause shape is set from the Shue model (Shue et al., 1997) with parameters $\alpha = 0.54$ and $r_0 = 10 R_E$, where α sets the level of flaring of the magnetopause flanks and r_0 defines the subsolar standoff distance. The lower left panel of Figure 4 displays an FFT of the field-aligned magnetic field component b_y at noon local time at $L = 8 R_E$ [$(\alpha, \beta, \gamma) = (8, 0, 0)$], for the initial storm phase equilibrium. We choose the compressional magnetic field component to study the fast mode, which has an antinode at local noon. There are two clear harmonics present at frequencies ~ 4.9 mHz and ~ 12 mHz (the frequency resolution of the FFT is 0.8 mHz). These are indicative of the natural fast modes of the simulation waveguide. A horizontal-dashed line at the fundamental frequency shown

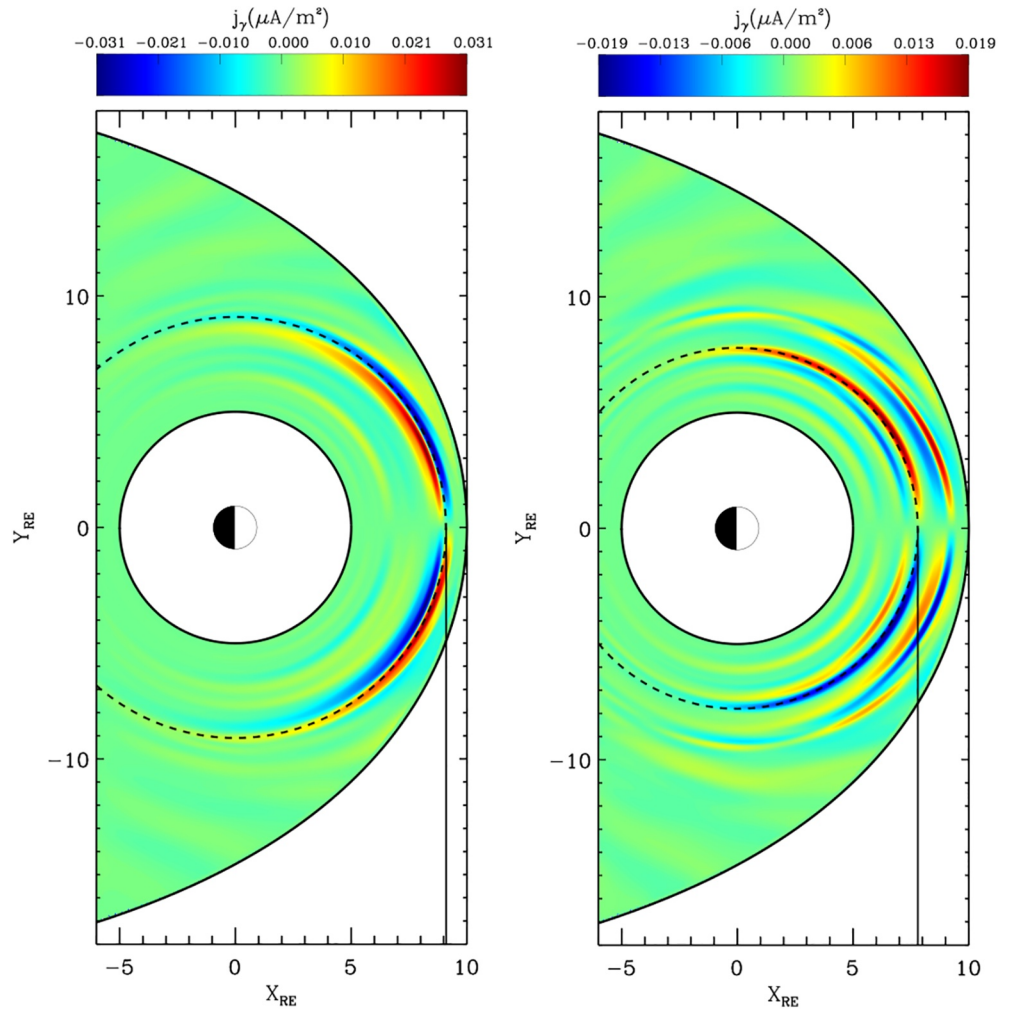


Figure 5. Color contours of field-aligned current density j_γ from near the ionospheric end of field lines, mapped to the equatorial plane. *Left:* Initial phase equilibrium, time $t = 20.19$ min. *Right:* Main phase equilibrium, time $t = 21.61$ min.

here (4.9 mHz) is overlaid onto the top panel, showing an expected FLR location (where fast and Alfvén frequencies match) at $L \sim 9.15 R_E$. The lower right figure displays an FFT of b_γ at the same location $((\alpha, \beta, \gamma) = (8, 0, 0))$ for the main phase equilibrium. Again two harmonics are present, at 4.3 mHz and ~ 11 mHz, with the fundamental overlaid on the top panel as the lower horizontal-dashed line, showing an expected FLR location of $L = 7.8 R_E$.

Figure 5 displays snapshots of the field-aligned current density j_γ from close to the ionospheric end of field lines, mapped along field lines to the equatorial plane (in a similar fashion to Figure 2). The left hand panel displays the results from the initial storm phase equilibrium, with a clear peak in the field-aligned current at $L \sim 9.1 R_E$, in keeping with the expected location as discussed in Figure 4. The right hand panel shows the main storm phase equilibrium results. There are two peaks in the field-aligned current distribution, with the inner at $L \sim 7.8 R_E$ corresponding to the fundamental mode and in agreement with the estimation from Figure 4. The FLR on outer L-shells around $L \sim 9 R_E$ represents a third harmonic field-aligned mode, excited by the second waveguide harmonic frequency of ~ 11 mHz. With phase motion over an Alfvén wave period, it should be noted that the peak locations in L-shell are confirmed by finding the average location of the maximum of $|j_\gamma|$ over a wave period.

4.3. Simulation With a $4 R_E$ Plasmapause and a $9 R_E$ Magnetopause

We now consider moving the simulation boundaries to $L = 4 R_E$ and $L = 9 R_E$, using the same Alfvén speed profiles as before in order to obtain the observed eigenfrequencies in the model. The distance between the

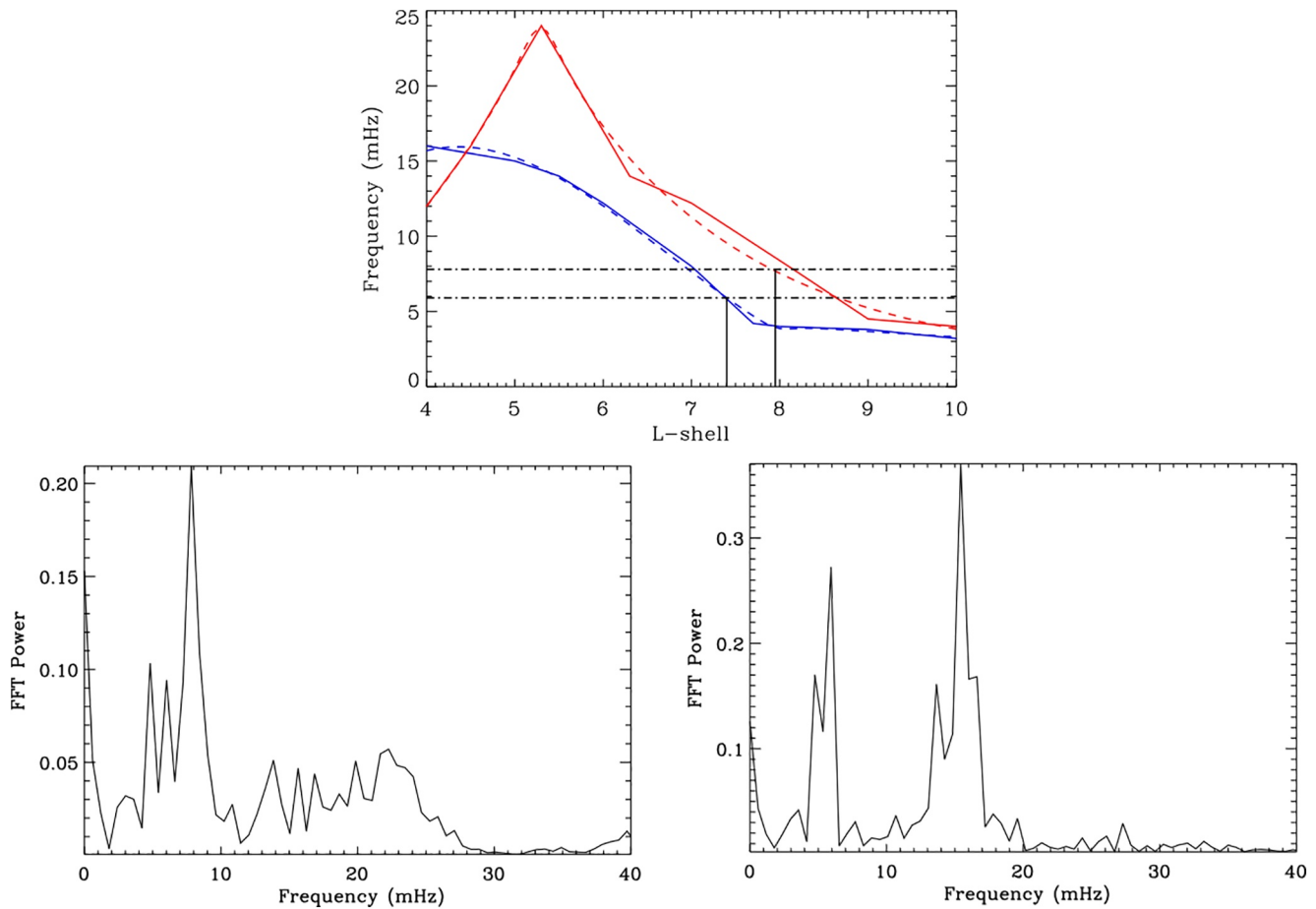


Figure 6. *Top:* Fits (dashed) to observed (solid) frequencies for initial (red) and main (blue) storm phases. Horizontal-dashed black lines represent model waveguide frequencies, with vertical lines showing expected FLR locations. *Bottom left:* FFT of field-aligned magnetic field component b_{\parallel} for the initial phase equilibrium, showing dominant waveguide frequency of $f \sim 8$ mHz. *Bottom right:* FFT b_{\parallel} for the main phase equilibrium, showing two waveguide harmonics at $f_1 \sim 6$ mHz and $f_2 \sim 15.5$ mHz.

plasmopause and subsolar magnetopause is maintained at $5 R_E$ for a consistent comparison. Figure 6 displays the frequency fits as well as the resulting waveguide frequencies in a similar manner to Figure 4. The lower panels show fundamental waveguide frequencies of $f \sim 8$ mHz for the initial storm phase equilibrium and $f \sim 6$ mHz for the main storm phase equilibrium. These frequencies are overlaid on the fits in the top panel, showing expected FLR locations at $L \sim 7.9 R_E$ for the initial phase and $L \sim 7.4 R_E$ for the main phase.

Figure 7 displays the field-aligned current density from close to the end of the field lines, mapped to the equatorial plane for the initial (left) and main (right) phase equilibria. It is clear that the FLR responses are again close to the predicted locations as per the top panel in Figure 6. It is interesting that in the right hand panel, there is not a stronger FLR response driven by the second waveguide harmonic, which is clearly present in the FFT in the lower right panel of Figure 6. There is a weak resonant response close to the inner boundary where the FLR driven at this second harmonic waveguide frequency would form, but it is dwarfed by that of the outer resonance. The inner resonance can be seen more clearly in the azimuthal velocity component (not shown) but is very faint in the field-aligned current response.

4.4. Combining Previous Simulations to Model a Storm Cycle

The real comparison to make is between the initial phase equilibrium with the boundaries further out (inner at $L = 5 R_E$, outer at $L = 10 R_E$), and the main phase equilibrium with the boundaries closer in (inner at $L = 4 R_E$, outer at $L = 9 R_E$). This accounts for the compression of the dayside magnetosphere as expected during the main

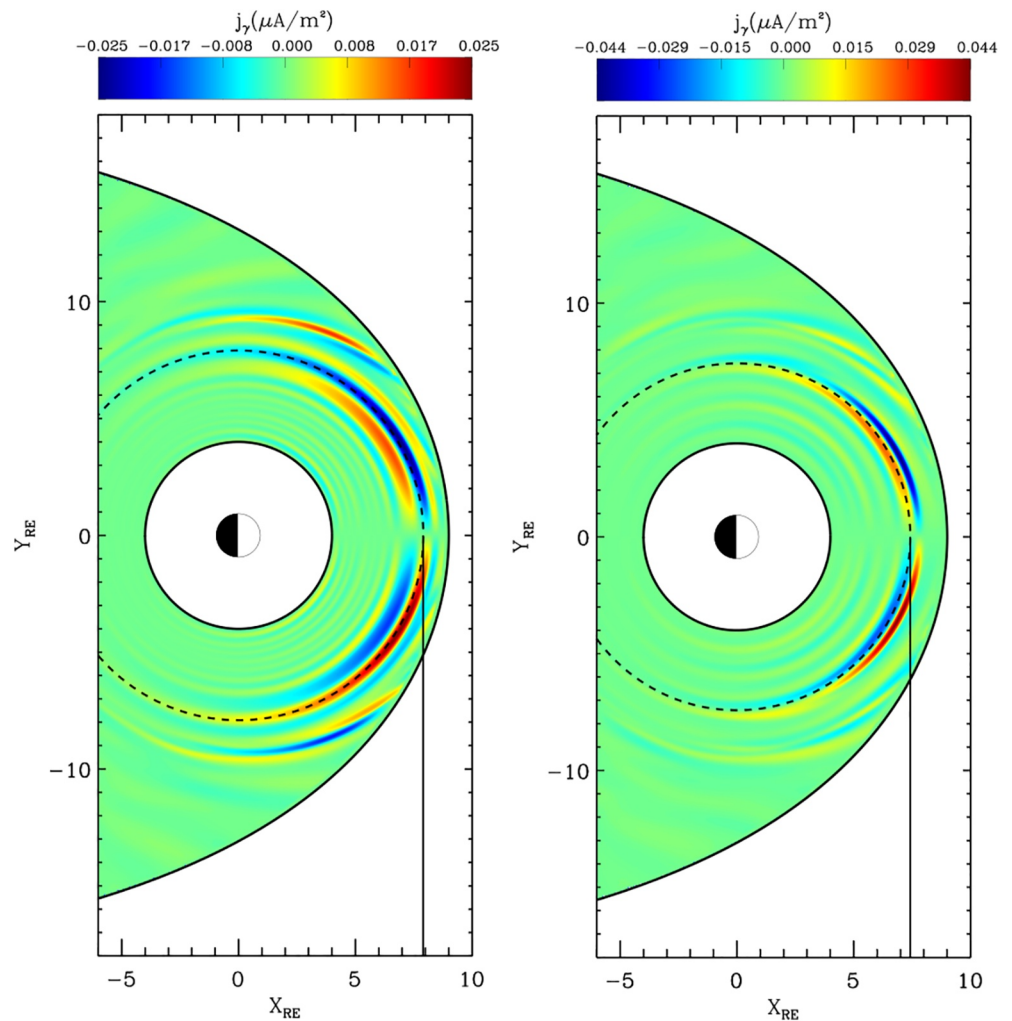


Figure 7. Color contours of field-aligned current density j_{γ} from near ionospheric end of field lines, mapped to the equatorial plane, for simulation boundaries at $L = 4 R_E$ and $L = 9 R_E$. *Left:* Initial phase equilibrium, time $t = 22.10$ min. *Right:* Main phase equilibrium, time $t = 22.43$ min.

phase of a geomagnetic storm. To this end, Figure 8 displays the left hand panel of Figure 5 and the right hand panel of Figure 7 together for comparison. The FLR location moves from $L \sim 9.1 R_E$ inward to $L \sim 7.4 R_E$. This is caused by two factors:

1. The waveguide frequency increases from $f \sim 4.9$ mHz to $f \sim 6$ mHz
2. The overall decrease in the Alfvén eigenfrequencies

5. Discussion

The results above elucidate many interesting elements of the fast-Alfvén wave coupling of the dayside magnetosphere during geomagnetic storms. The key idea to convey is the concept of the two resonance system; namely, the resonance of the fast waveguide modes excited by broadband solar wind driving, which then go on to excite discrete frequency FLRs. Therefore the frequency, structure, and location of the resulting FLRs are inextricably linked to that of the fast waveguide normal modes. These modes will depend upon the magnetic field structure, plasma mass density variation and the size and shape of the magnetospheric waveguide and will therefore result in a broad spectrum of permissible frequencies. The particular fast waveguide modes excited will further depend upon the temporal/spatial structure of the solar wind driving (Elsden & Wright, 2019).

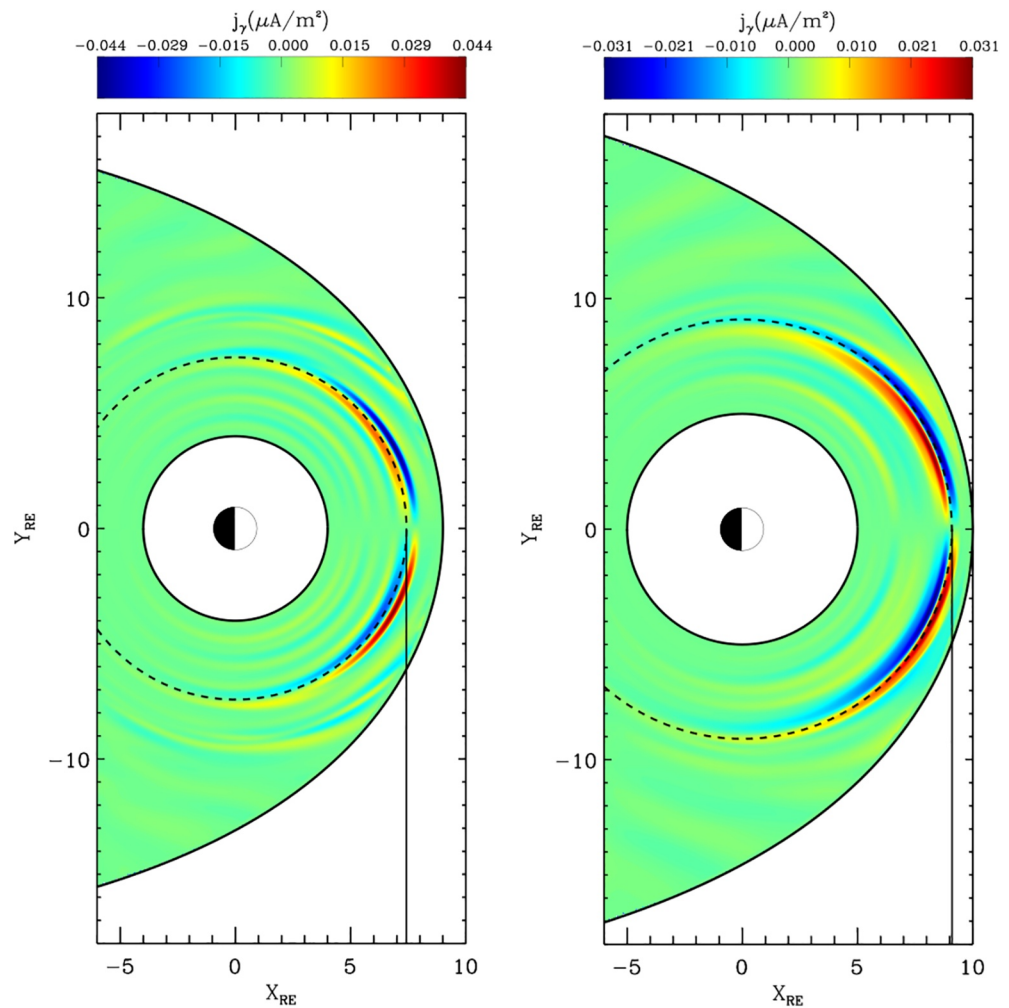


Figure 8. Color contours of field-aligned current j_γ , copied figures from *Left*: Figure 5 left panel; *Right*: Figure 7 right panel, for comparison.

The equilibria that we have used to model the observed Alfvén eigenfrequencies, with a fixed dipole magnetic field, will evidently not capture all of the complexity of the storm time magnetosphere. Furthermore, we have had to make assumptions about the frequency profiles beyond the furthest observed L-shell. Therefore, specific values of the waveguide frequencies presented should not be taken as exactly representative of observations of such modes. What is important however, is the relative change to these waveguide frequencies upon varying the plasma mass density structure and the plasmopause/magnetopause locations. For the modest average storm conditions used here, we see a 20% increase in the waveguide frequency by moving the boundaries inward by only $1R_E$ (and maintaining the same waveguide width of $5R_E$ along the noon meridian). This, combined with the overall decrease in the Alfvén eigenfrequencies, creates a significant variation in FLR locations. During a severe storm, it would be expected that the enhanced dayside compression will substantially shrink the width of the waveguide. For example, during the March 2013 storm, Staples et al. (2020) observed the magnetopause to be compressed within geostationary orbit ($L \sim 6.6 R_E$). Le et al. (2016) similarly observed magnetopause crossings with the GOES spacecraft (at geostationary orbit) during the 17 March 2015 storm. With such a compressed magnetopause, Murphy et al. (2015) demonstrated that ULF wave power will increase and will penetrate to lower L . As for the plasmopause, Obana et al. (2019) recorded a plasmopause location inside of $L = 2$ for the September 2017 storm. Such extreme boundary dislocations would act to significantly increase the waveguide frequency and could move the FLRs substantially Earthward. Such observations are in keeping with the formation of FLRs at low L values during the magnetic storm of 24 March 1991 (E. A. Lee et al., 2007). However, as described in the

introductory Sections 1.2 and 1.3, the storm time heavy ion dynamics will have a substantial effect on the overall plasma mass density, which would have to be taken into account when studying such extreme cases.

The FLR locations presented in the simulations are still at reasonably large L , particularly if interested in the potential interaction with radiation belt particles, with the heart of the outer belt usually residing around $L \sim 4$ (Horne et al., 2005). We have mostly looked at the fundamental waveguide mode (quarter radial wavelength with the given boundary conditions), however considering higher waveguide mode harmonics would lead to FLR formation further Earthward. Such excitation is partly visible in several of the current density plots, for example, both panels of Figures 5 and 7 show weaker FLR peaks Earthward of the dominant FLR. As mentioned above, the important aspect of this modeling work is the overall trend of more Earthward FLR formation during the storm main phase, not the specific FLR locations themselves. It should be stressed that our modeling work only treats the region $L > 4$, mostly outside of the plasmopause. Interestingly, at locations inside of the initial phase plasmopause, it may be expected that FLRs actually move radially outward by the main phase. As shown in the statistical study of Wharton et al. (2020), for $L < 4$ the eigenfrequencies increase from initial to main phase. Therefore coupling to a FLR for a given fast mode frequency would be expected to occur at larger L during the main phase for $L < 4$. It has also been previously suggested that the largest FLRs occur outside of the plasmopause, with the wave amplitudes being smaller inside (Balasis et al., 2015). This provides further motivation for the region of focus of this study, as well as its relevance to radiation belt studies, in particular when the plasmopause reaches very low L (e.g., Obana et al., 2019).

An aspect not addressed in this study is the ability of fast mode waves to penetrate deeper into the magnetosphere based on the depressed Alfvén continuum (Loto'aniu et al., 2006; E. A.; Lee et al., 2007; Rae et al., 2019). It has been previously shown that overall ULF wave power in the Pc5 band ($\sim 1 - 10$ MHz) decays exponentially with decreasing L (Mathie & Mann, 2001). In our simulations, we have studied the fundamental waveguide modes of the dayside magnetosphere, which span the full radial extent from the plasmopause to magnetopause. In order to reconcile this with statistical observations of overall ULF wave power, an ensemble of simulations would have to be run, encompassing the varying states of the magnetosphere, then be statistically averaged, which is beyond the scope of this study.

Further of interest regarding wave-particle interactions are the FLR widths presented in the simulations. It can be seen clearly, for example, in Figure 7, that the FLR widths vary from the initial (left) to main (right) phase. The change of the resonance width in time is determined primarily by the phase-mixing length, $L_{ph} \sim 2\pi / (v\omega'_A(L))$ (Mann et al., 1995; where the prime superscript denotes d/dL , and ω_A is the local Alfvén frequency), which can be seen to depend critically upon the radial Alfvén frequency gradient. The steady state resonance width is limited by the dissipation in the system, which in our model is provided by the inclusion of resistivity. Consider the FLR widths in Figure 7. It is clear that the right panel for the main phase equilibria has a thinner width than that for the initial phase (left). This occurs because for this resonance location, the local Alfvén frequency gradient is steeper. This is evident by comparing the gradients of the red and blue curves in the top panel of Figure 6 at the FLR locations (vertical black lines). Under different geomagnetic conditions, the shape of the Alfvén speed (and therefore frequency) profile can vary drastically (Archer et al., 2015, 2017). Given it is the local Alfvén frequency gradient which determines the FLR width, we cannot make any generalisations regarding the systematic FLR width variation during storm phases. Furthermore, we have used a statistical average of the frequency over 132 storms, which may not accurately depict individual cases. Another related point is the FLR amplitude, which is proportional to the inverse of the Alfvén frequency gradient (Wright & Thompson, 1994). Both the width and the amplitude are important features for wave-particle interactions, defining the region across which the ULF wave exists (and thus the radial extent in which particles can be accelerated) as well as the potential strength of the interaction. Therefore, it would be expected that a shallower Alfvén frequency gradient would provide a more efficient regime for enhanced wave-particle interactions.

A follow up study will consider the full magnetic local time asymmetries as present in the current and many previous observations (Takahashi et al., 2016; Walach et al., 2021; Wharton et al., 2018). The formation of a plasmaspheric drainage plume on the dusk flank during storms has been shown to significantly alter the propagation characteristics of ULF waves (Degeling et al., 2018). This has the potential even to form cavity modes of the plume itself. Further asymmetries could also be introduced through asymmetric magnetopause driving, which would significantly impact the waveguide modes that are preferentially excited (Wright & Elsdén, 2020). Furthermore, with asymmetric density structures comes the requirement of 3D FLR theory to account for mixed

polarisation FLRs (Elsden & Wright, 2017; Wright & Elsden, 2016). Wright et al. (2018) explored how such azimuthal density gradients cause the refraction of fast mode waves, which in turn can be used as part of the explanation for the dawn-side enhancement in toroidal Pc5 waves (Takahashi et al., 2016).

6. Conclusions

This study has assessed how the location of field line resonances in the plasmatrough varies with different phases of a geomagnetic storm. This has been achieved through MHD simulations specifically tailored for resolving the fine perpendicular scales appearing during the FLR process. We have used observed radial eigenfrequency profiles for the initial and main storm phases, averaged over 132 geomagnetic storms as input for the simulation equilibria. We performed four simulations, for two different inner/outer boundary locations and two different radial frequency profiles (for initial/main phase). The key findings are as follows:

1. FLR location is dependent upon the Alfvén frequency continuum and the waveguide mode frequency (which is driving the FLR)—factors which must be considered together.
2. The overall decrease in Alfvén frequency outside the plasmasphere from the initial to main storm phase, without considering changing magnetopause/plasmapause locations, would result in a decrease of the natural fast waveguide frequency excited through broadband magnetopause driving.
3. However, including a very modest change of $1 R_E$ to the magnetopause/plasmapause boundary locations (but maintaining a plasmapause to magnetopause distance of $5 R_E$ along the noon meridian) causes the fast waveguide frequency to *increase* over the course of a storm. This is most likely caused by the overall higher Alfvén speed regions sampled in the more Earthward waveguide.
4. The combined effects of a higher fast waveguide frequency and lower Alfvén frequencies during the storm main phase, act together to move resonance locations outside the plasmasphere considerably Earthward, by $\sim 1.7 R_E$ for the moderate storm environments considered in this study.
5. Such interplay of the waveguide mode frequency and the Alfvén continuum over the course of a storm requires a more nuanced analysis than simply assuming a given fast frequency, then finding the resulting FLR location. Our results here expand upon the ideas of Rae et al. (2019), who considered how different frequency fast mode waves could penetrate into the inner magnetosphere during storms.
6. The ideas developed here could potentially be extrapolated for extreme storms, where the boundaries and Alfvén continuum are substantially different to those considered here. We would expect increased waveguide frequencies and far more inward FLR formation (e.g., $L \sim 3.6 R_E$; E. A. Lee et al., 2007) than shown in our results. However, heavy ions and their effect on the plasma mass density would also need to be appropriately accounted for in these situations

Data Availability Statement

Data used to produce the simulation plots can be accessed at this site (https://figshare.com/authors/Tom_Elsden/4743264). The authors would like to thank the IMAGE magnetometer team for providing the data.

Acknowledgments

T. Elsden was supported by a Leverhulme Trust Early Career Fellowship (ECF-2019-155), the University of Leicester and the University of Glasgow. I. J. Rae was supported by NERC Grants NE/P017185/1 and NE/V002554/2 and STFC Grant ST/V006320/1. T. K. Yeoman and M. K. James were supported by STFC Grant ST/S000429/1. J. K. Sandhu was supported by NERC Grants NE/P017185/2 and NE/V002554/2. M-T Walach was supported by NERC Grant NE/T000937/1. This research used the SPECTRE High Performance Computing Facility at the University of Leicester.

References

- Akasofu, S. I., Chapman, S., & Venkatesan, B. (1963). The main phase of great magnetic storms. *Journal of Geophysical Research*, *68*(11), 3345–3350. <https://doi.org/10.1029/JZ068i011p03345>
- Alfvén, H. (1942). Existence of electromagnetic-hydrodynamic waves. *Nature*, *150*, 405–406. <https://doi.org/10.1038/150405d0>
- Allan, W., White, S. P., & Poulter, E. M. (1985). Magnetospheric coupling of hydromagnetic waves - initial results. *Geophysical Research Letters*, *12*, 287–290. <https://doi.org/10.1029/GL012i005p00287>
- Allan, W., White, S. P., & Poulter, E. M. (1986). Impulse-excited hydromagnetic cavity and field-line resonances in the magnetosphere. *Planetary and Space Science*, *34*, 371–385. [https://doi.org/10.1016/0032-0633\(86\)90144-3](https://doi.org/10.1016/0032-0633(86)90144-3)
- Archer, M. O., Hartinger, M. D., Walsh, B. M., & Angelopoulos, V. (2017). Magnetospheric and solar wind dependences of coupled fast-mode resonances outside the plasmasphere. *Journal of Geophysical Research*, *122*, 212–226. <https://doi.org/10.1002/2016JA023428>
- Archer, M. O., Hartinger, M. D., Walsh, B. M., Plaschke, F., & Angelopoulos, V. (2015). Frequency variability of standing Alfvén waves excited by fast mode resonances in the outer magnetosphere. *Geophysical Research Letters*, *42*, 10. <https://doi.org/10.1002/2015GL066683>
- Balasis, G., Daglis, I. A., Mann, I. R., Papadimitriou, C., Zesta, E., Georgiou, M., et al. (2015). Multi-satellite study of the excitation of Pc3 and Pc4-5 ULF waves and their penetration across the plasmapause during the 2003 Halloween superstorm. *Annales Geophysicae*, *33*(10), 1237–1252. <https://doi.org/10.5194/angeo-33-1237-2015>
- Baranskii, L. N., Borovkov, I. E., Gokhberg, M. B., Krylov, S. M., & Troitskaia, V. A. (1985). High resolution method of direct measurement of the magnetic field lines' eigen frequencies. *Planetary and Space Science*, *33*(12), 1369–1374. [https://doi.org/10.1016/0032-0633\(85\)90112-6](https://doi.org/10.1016/0032-0633(85)90112-6)

- Berube, D., Moldwin, M. B., & Weygand, J. M. (2003). An automated method for the detection of field line resonance frequencies using ground magnetometer techniques. *Journal of Geophysical Research*, *108*, 1348. <https://doi.org/10.1029/2002JA009737>
- Chen, L., & Hasegawa, A. (1974). A theory of long-period magnetic pulsations: I. Steady state excitation of field line resonance. *Journal of Geophysical Research*, *79*, 1024–1032. <https://doi.org/10.1029/JA079i007p01024>
- Chi, P. J., Lee, D.-H., & Russell, C. T. (2006). Tamao travel time of sudden impulses and its relationship to ionospheric convection vortices. *Journal of Geophysical Research: Space Physics*, *111*(A8). <https://doi.org/10.1029/2005ja011578>
- Chi, P. J., Russell, C. T., Foster, J. C., Moldwin, M. B., Engebretson, M. J., & Mann, I. R. (2005, January). Density enhancement in plasmasphere-ionosphere plasma during the 2003 Halloween Superstorm: Observations along the 330th magnetic meridian in North America. *Geophysical Research Letters*, *32*(3), L03S07. <https://doi.org/10.1029/2004GL021722>
- Claudepierre, S. G., Mann, I. R., Takahashi, K., Fennell, J. F., Hudson, M. K., Blake, J. B., et al. (2013). Van allen probes observation of localized drift resonance between poloidal mode ultra-low frequency waves and 60 keV electrons. *Geophysical Research Letters*, *40*(17), 4491–4497. <https://doi.org/10.1002/grl.50901>
- Corpo, A., Heilig, B., Pietropaolo, E., Reda, J., & Lichtenberger, J. (2019). Observing the cold plasma in the earth's magnetosphere with the EMMA network. *Annals of geophysics*, *62*(4), GM447. <https://doi.org/10.4401/ag-7751>
- Degeling, A. W., Rae, I. J., Watt, C. E. J., Shi, Q. Q., Rankin, R., & Zong, Q. G. (2018). Control of ULF wave accessibility to the inner magnetosphere by the convection of plasma density. *Journal of Geophysical Research*, *123*(2), 1086–1099. <https://doi.org/10.1002/2017JA024874>
- Degeling, A. W., Rankin, R., Kabin, K., Marchand, R., & Mann, I. R. (2007). The effect of ULF compressional modes and field line resonances on relativistic electron dynamics. *Planetary and Space Science*, *55*(6), 731–742. <https://doi.org/10.1016/j.pss.2006.04.039>
- de Moura, C., & Kubrusly, C. (2013). *The Courant–Friedrichs–Lewy (CFL) condition*. Springer. <https://doi.org/10.1007/978-0-8176-8394-8>
- Dent, Z. C., Mann, I. R., Goldstein, J., Menk, F. W., & Ozeke, L. G. (2006). Plasmaspheric depletion, refilling, and plasmopause dynamics: A coordinated ground-based and IMAGE satellite study. *Journal of Geophysical Research*, *111*(A3), A03205. <https://doi.org/10.1029/2005JA011046>
- Dungey, J. W. (1955). Electrodynamics of the outer atmosphere. *Physics of the ionosphere*, 229.
- Dungey, J. W. (1961). Interplanetary magnetic field and the auroral zones. *Physical Review Letters*, *6*, 47–48. <https://doi.org/10.1103/PhysRevLett.6.47>
- Elkington, S. R., Hudson, M. K., & Chan, A. A. (1999). Acceleration of relativistic electrons via drift-resonant interaction with toroidal-mode Pc-5 ULF oscillations. *Geophysical Research Letters*, *26*(21), 3273–3276. <https://doi.org/10.1029/1999GL003659>
- Elkington, S. R., Hudson, M. K., & Chan, A. A. (2003). Resonant acceleration and diffusion of outer zone electrons in an asymmetric geomagnetic field. *Journal of Geophysical Research*, *108*(A3), 1116. <https://doi.org/10.1029/2001JA009202>
- Elsden, T., & Wright, A. N. (2017). The theoretical foundation of 3-D Alfvén resonances: Time-dependent solutions. *Journal of Geophysical Research*, *122*, 3247–3261. <https://doi.org/10.1002/2016JA023811>
- Elsden, T., & Wright, A. N. (2019). The effect of fast normal mode structure and magnetopause forcing on FLRs in a 3-D waveguide. *Journal of Geophysical Research*, *124*(1), 178–196. <https://doi.org/10.1029/2018JA026222>
- Foster, J. C., Wygant, J. R., Hudson, M. K., Boyd, A. J., Baker, D. N., Erickson, P. J., & Spence, H. E. (2015). Shock-induced prompt relativistic electron acceleration in the inner magnetosphere. *Journal of Geophysical Research: Space Physics*, *120*(3), 1661–1674. <https://doi.org/10.1002/2014ja020642>
- Fraser, B. J., Horwitz, J. L., Slavin, J. A., Dent, Z. C., & Mann, I. R. (2005). Heavy ion mass loading of the geomagnetic field near the plasmapause and ULF wave implications. *Geophysical Research Letters*, *32*(4). <https://doi.org/10.1029/2004gl021315>
- Gkioulidou, M., Ohtani, S., Ukhorskiy, A. Y., Mitchell, D. G., Takahashi, K., Spence, H. E., et al. (2019). Low-energy (<keV) O⁺ ion outflow directly into the inner magnetosphere: Van allen probes observations. *Journal of Geophysical Research: Space Physics*, *124*(1), 405–419. <https://doi.org/10.1029/2018ja025862>
- Gonzalez, W. D., Joselyn, J. A., Kamide, Y., Kroehl, H. W., Rostoker, G., Tsurutani, B. T., & Vasyliunas, V. M. (1994). What is a geomagnetic storm? *Journal of Geophysical Research: Space Physics*, *99*(A4), 5771–5792. <https://doi.org/10.1029/93ja02867>
- Hao, Y. X., Zong, Q.-G., Zhou, X.-Z., Rankin, R., Chen, X. R., Liu, Y., et al. (2019). Global-scale ULF waves associated with SSC accelerate magnetospheric ultrarelativistic electrons. *Journal of Geophysical Research: Space Physics*, *124*(3), 1525–1538. <https://doi.org/10.1029/2018ja026134>
- Hartinger, M., Angelopoulos, V., Moldwin, M. B., Glassmeier, K.-H., & Nishimura, Y. (2011). Global energy transfer during a magnetospheric field line resonance. *Geophysical Research Letters*, *38*, L12101. <https://doi.org/10.1029/2011GL047846>
- Herlofson, N. (1950). Magneto-hydrodynamic waves in a compressible fluid conductor. *Nature*, *165*(4208), 1020–1021. <https://doi.org/10.1038/1651020a0>
- Horne, R. B., Thorne, R. M., Shprits, Y. Y., Meredith, N. P., Glauert, S. A., Smith, A. J., et al. (2005). Wave acceleration of electrons in the Van Allen radiation belts. *Nature*, *437*(7056), 227–230. <https://doi.org/10.1038/nature03939>
- Hutchinson, J. A., Wright, D. M., & Milan, S. E. (2011). Geomagnetic storms over the last solar cycle: A superposed epoch analysis. *Journal of Geophysical Research: Space Physics*, *116*(A9). <https://doi.org/10.1029/2011JA016463>
- Inhester, B. (1987). Numerical modeling of hydromagnetic wave coupling in the magnetosphere. *Journal of Geophysical Research*, *92*, 4751–4756. <https://doi.org/10.1029/JA092iA05p04751>
- Iyemori, T. (1990). Storm-time magnetospheric currents inferred from mid-latitude geomagnetic field variations. *Journal of Geomagnetism and Geoelectricity*, *42*(11), 1249–1265. <https://doi.org/10.5636/jgg.42.1249>
- Jacobs, J. A., Kato, Y., Matsushita, S., & Troitskaya, V. A. (1964). Classification of geomagnetic micropulsations. *Journal of Geophysical Research*, *69*, 180–181. <https://doi.org/10.1029/JZ069i001p00180>
- Kageyama, A., Sugiyama, T., Watanabe, K., & Sato, T. (2006). A note on the dipole coordinates. *Computers & Geosciences*, *32*, 265–269. <https://doi.org/10.1016/j.cageo.2005.06.006>
- Kale, Z. C., Mann, I. R., Waters, C. L., Vellante, M., Zhang, T. L., & Honary, F. (2009). Plasmaspheric dynamics resulting from the Halloween 2003 geomagnetic storms. *Journal of Geophysical Research*, *114*(A8), A08204. <https://doi.org/10.1029/2009JA014194>
- Kivelson, M. G., & Southwood, D. J. (1985). Resonant ULF waves - a new interpretation. *Geophysical Research Letters*, *12*, 49–52. <https://doi.org/10.1029/GL012i001p00049>
- Kivelson, M. G., & Southwood, D. J. (1986). Coupling of global magnetospheric MHD eigenmodes to field line resonances. *Journal of Geophysical Research*, *91*, 4345–4351. <https://doi.org/10.1029/JA091iA04p04345>
- Kozyra, J. U., Jordanova, V. K., Borovsky, J. E., Thomsen, M. F., Knipp, D. J., Evans, D. S., et al. (1998). Effects of a high-density plasma sheet on ring current development during the november 2–6, 1993, magnetic storm. *Journal of Geophysical Research: Space Physics*, *103*(A11), 26285–26305. <https://doi.org/10.1029/98ja01964>

- Li, X.-Y., Liu, Z.-Y., Zong, Q.-G., Zhou, X.-Z., Hao, Y.-X., Rankin, R., & Zhang, X.-X. (2021). Pitch angle phase shift in ring current ions interacting with ultra-low-frequency waves: Van allen probes observations. *Journal of Geophysical Research: Space Physics*, *126*(4), e2020JA029025. <https://doi.org/10.1029/2020JA029025>
- Lee, D.-H., & Lysak, R. L. (1989). Magnetospheric ULF wave coupling in the dipole model - the impulsive excitation. *Journal of Geophysical Research*, *94*, 17097–17103. <https://doi.org/10.1029/JA094iA12p17097>
- Lee, E. A., Mann, I. R., Loto'aniu, T. M., & Dent, Z. C. (2007). Global Pc5 pulsations observed at unusually low L during the great magnetic storm of 24 March 1991. *Journal of Geophysical Research*, *112*(A5), A05208. <https://doi.org/10.1029/2006JA011872>
- Le, G., Lühr, H., Anderson, B. J., Strangeway, R. J., Russell, C. T., Singer, H., et al. (2016). Magnetopause erosion during the 17 march 2015 magnetic storm: Combined field-aligned currents, auroral oval, and magnetopause observations. *Geophysical Research Letters*, *43*(6), 2396–2404. <https://doi.org/10.1002/2016gl068257>
- Liu, Z.-Y., Zong, Q.-G., Zhou, X.-Z., Hao, Y. X., Yau, A. W., Zhang, H., et al. (2019). Ulf waves modulating and acting as mass spectrometer for dayside ionospheric outflow ions. *Geophysical Research Letters*, *46*(15), 8633–8642. <https://doi.org/10.1029/2019gl083849>
- Liu, Z.-Y., Zong, Q.-G., Zhou, X.-Z., Zhu, Y.-F., & Gu, S.-J. (2020). Pitch angle structures of ring current ions induced by evolving poloidal ultra-low frequency waves. *Geophysical Research Letters*, *47*(4), e2020GL087203. <https://doi.org/10.1029/2020GL087203>
- Loto'aniu, T. M., Mann, I. R., Ozeke, L. G., Chan, A. A., Dent, Z. C., & Milling, D. K. (2006). Radial diffusion of relativistic electrons into the radiation belt slot region during the 2003 halloween geomagnetic storms. *Journal of Geophysical Research: Space Physics*, *111*(A4). <https://doi.org/10.1029/2005JA011872>
- Lühr, H. (1994). The image magnetometer network. *STEP International Newsletter*, *4*, 4–6.
- Mann, I. R., Lee, E. A., Claudepierre, S. G., Fennell, J. F., Degeling, A., Rae, I. J., et al. (2013). Discovery of the action of a geophysical synchrotron in the Earth's Van Allen radiation belts. *Nature Communications*, *4*, 2795. <https://doi.org/10.1038/ncomms3795>
- Mann, I. R., Wright, A. N., & Cally, P. S. (1995). Coupling of magnetospheric cavity modes to field line resonances: A study of resonance widths. *Journal of Geophysical Research*, *100*, 19441–19456. <https://doi.org/10.1029/95JA00820>
- Mann, I. R., Wright, A. N., Mills, K. J., & Nakariakov, V. M. (1999). Excitation of magnetospheric waveguide modes by magnetosheath flows. *Journal of Geophysical Research*, *104*, 333–353. <https://doi.org/10.1029/1998JA900026>
- Mathie, R. A., & Mann, I. R. (2001). On the solar wind control of pc5 ULF pulsation power at mid-latitudes: Implications for MeV electron acceleration in the outer radiation belt. *Journal of Geophysical Research: Space Physics*, *106*(A12), 29783–29796. <https://doi.org/10.1029/2001ja000002>
- Menk, F., Kale, Z., Sciffer, M., Robinson, P., Waters, C., Grew, R., et al. (2014). Remote sensing the plasmasphere, plasmopause, plumes and other features using ground-based magnetometers. *Journal of Space Weather and Space Climate*, *4*, A34. <https://doi.org/10.1051/swsc/2014030>
- Menk, F. W., Orr, D., Clilverd, M. A., Smith, A. J., Waters, C. L., Milling, D. K., & Fraser, B. J. (1999). Monitoring spatial and temporal variations in the dayside plasmasphere using geomagnetic field line resonances. *Journal of Geophysical Research: Space Physics*, *104*(A9), 19955–19969. <https://doi.org/10.1029/1999ja900205>
- Milan, S. E., Sato, N., Ejiri, M., & Moen, J. (2001). Auroral forms and the field-aligned current structure associated with field line resonances. *Journal of Geophysical Research*, *106*(A11), 25825–25833. <https://doi.org/10.1029/2001JA900077>
- Murphy, K. R., Mann, I. R., & Ozeke, L. G. (2014). A ULF wave driver of ring current energization. *Geophysical Research Letters*, *41*(19), 6595–6602. <https://doi.org/10.1002/2014GL061253>
- Murphy, K. R., Mann, I. R., & Sibeck, D. G. (2015). On the dependence of storm time ULF wave power on magnetopause location: Impacts for ULF wave radial diffusion. *Geophysical Research Letters*, *42*(22), 9676–9684. <https://doi.org/10.1002/2015GL066592>
- Murphy, K. R., Watt, C. E. J., Mann, I. R., Jonathan Rae, I., Sibeck, D. G., Boyd, A. J., et al. (2018). The global statistical response of the outer radiation belt during geomagnetic storms. *Geophysical Research Letters*, *45*(9), 3783–3792. <https://doi.org/10.1002/2017gl076674>
- Obana, Y., Maruyama, N., Shinbori, A., Hashimoto, K. K., Fedrizzi, M., Nosé, M., et al. (2019). Response of the ionosphere-plasmasphere coupling to the september 2017 storm: What erodes the plasmasphere so severely? *Space Weather*, *17*(6), 861–876. <https://doi.org/10.1029/2019sw002168>
- O'Brien, T. P., & Moldwin, M. B. (2003). Empirical plasmapause models from magnetic indices. *Geophysical Research Letters*, *30*(4). <https://doi.org/10.1029/2002GL015400>
- Oimatsu, S., Nosé, M., Teramoto, M., Yamamoto, K., Matsuoka, A., Kasahara, S., et al. (2018). Drift-bounce resonance between pc5 pulsations and ions at multiple energies in the nightside magnetosphere: Arase and mms observations. *Geophysical Research Letters*, *45*(15), 7277–7286. <https://doi.org/10.1029/2018gl078961>
- Radoski, H. R. (1967). A note on oscillating field lines. *Journal of Geophysical Research*, *72*, 418–419. <https://doi.org/10.1029/JZ072i001p00418>
- Rae, I. J., Donovan, E. F., Mann, I. R., Fenrich, F. R., Watt, C. E. J., Milling, D. K., et al. (2005). Evolution and characteristics of global Pc5 ULF waves during a high solar wind speed interval. *Journal of Geophysical Research*, *110*, A12211. <https://doi.org/10.1029/2005JA011007>
- Rae, I. J., Murphy, K. R., Watt, C. E. J., Sandhu, J. K., Georgiou, M., Degeling, A. W., et al. (2019). How do ultra-low frequency waves access the inner magnetosphere during geomagnetic storms? *Geophysical Research Letters*, *46*(19), 10,699–10,10709. <https://doi.org/10.1029/2019GL082395>
- Rankin, R., Kabin, K., Lu, J. Y., Mann, I. R., Marchand, R., Rae, I. J., & Donovan, E. F. (2005). Magnetospheric field-line resonances: Ground-based observations and modeling. *Journal of Geophysical Research*, *110*(A10), A10S09. <https://doi.org/10.1029/2004JA010919>
- Roberts, W. T., Jr, Horwitz, J. L., Comfort, R. H., Chappell, C. R., Waite, J. H., Jr, & Green, J. L. (1987). Heavy ion density enhancements in the outer plasmasphere. *Journal of Geophysical Research: Space Physics*, *92*(A12), 13499–13512. <https://doi.org/10.1029/JA092iA12p13499>
- Samson, J. C., Harrold, B. G., Ruohoniemi, J. M., Greenwald, R. A., & Walker, A. D. M. (1992). Field line resonances associated with MHD waveguides in the magnetosphere. *Geophysical Research Letters*, *19*, 441–444. <https://doi.org/10.1029/92GL00116>
- Samson, J. C., Jacobs, J. A., & Rostoker, G. (1971). Latitude-dependent characteristics of long-period geomagnetic micropulsations. *Journal of Geophysical Research*, *76*, 3675–3683. <https://doi.org/10.1029/JA076i016p03675>
- Sandhu, J. K., Yeoman, T. K., & Rae, I. J. (2018). Variations of field line eigenfrequencies with ring current intensity. *Journal of Geophysical Research*, *123*(11), 9325–9339. <https://doi.org/10.1029/2018JA025751>
- Sandhu, J. K., Yeoman, T. K., Rae, I. J., Fear, R. C., & Dandouras, I. (2017). The dependence of magnetospheric plasma mass loading on geomagnetic activity using Cluster. *Journal of Geophysical Research*, *122*, 9371–9395. <https://doi.org/10.1002/2017JA024171>
- Shen, X.-C., Shi, Q., Wang, B., Zhang, H., Hudson, M. K., Nishimura, Y., et al. (2018). Dayside magnetospheric and ionospheric responses to a foreshock transient on 25 June 2008: 1. Flr observed by satellite and ground-based magnetometers. *Journal of Geophysical Research: Space Physics*, *123*(0), 6335–6346. <https://doi.org/10.1029/2018JA025349>
- Shue, J. H., Chao, J. K., Fu, H. C., Russell, C. T., Song, P., Khurana, K. K., & Singer, H. J. (1997). A new functional form to study the solar wind control of the magnetopause size and shape. *Journal of Geophysical Research*, *102*(A5), 9497–9511. <https://doi.org/10.1029/97JA00196>
- Singer, H. J., Southwood, D. J., Walker, R. J., & Kivelson, M. G. (1981). Alfven wave resonances in a realistic magnetospheric magnetic field geometry. *Journal of Geophysical Research*, *86*, 4589–4596. <https://doi.org/10.1029/JA086iA06p04589>

- Southwood, D. J. (1968). The hydromagnetic stability of the magnetospheric boundary. *Planetary and Space Science*, 16, 587–605. [https://doi.org/10.1016/0032-0633\(68\)90100-1](https://doi.org/10.1016/0032-0633(68)90100-1)
- Southwood, D. J. (1974). Some features of field line resonances in the magnetosphere. *Planetary and Space Science*, 22, 483–491. [https://doi.org/10.1016/0032-0633\(74\)90078-6](https://doi.org/10.1016/0032-0633(74)90078-6)
- Southwood, D. J., Dungey, J. W., & Etherington, R. J. (1969). Bounce resonant interaction between pulsations and trapped particles. *Planetary and Space Science*, 17(3), 349–361. [https://doi.org/10.1016/0032-0633\(69\)90068-3](https://doi.org/10.1016/0032-0633(69)90068-3)
- Southwood, D. J., & Kivelson, M. G. (1981). Charged particle behavior in low-frequency geomagnetic pulsations 1. Transverse waves. *Journal of Geophysical Research*, 86(A7), 5643–5655. <https://doi.org/10.1029/JA086iA07p05643>
- Southwood, D. J., & Kivelson, M. G. (1982). Charged particle behavior in low-frequency geomagnetic pulsations 2. Graphical approach. *Journal of Geophysical Research*, 87(A3), 1707–1710. <https://doi.org/10.1029/JA087iA03p01707>
- Staples, F. A., Rae, I. J., Forsyth, C., Smith, A. R. A., Murphy, K. R., Raymer, K. M., et al. (2020). Do statistical models capture the dynamics of the magnetopause during sudden magnetospheric compressions? *Journal of Geophysical Research: Space Physics*, 125(4), e2019JA027289. <https://doi.org/10.1029/2019JA027289>
- Takahashi, K., Denton, R. E., Anderson, R. R., & Hughes, W. J. (2006). Mass density inferred from toroidal wave frequencies and its comparison to electron density. *Journal of Geophysical Research*, 111(A1), A01201. <https://doi.org/10.1029/2005JA011286>
- Takahashi, K., Denton, R. E., & Gallagher, D. (2002). Toroidal wave frequency at L = 6–10: Active Magnetospheric Particle Tracer Explorers/CCE observations and comparison with theoretical model. *Journal of Geophysical Research*, 107(A2), SMP2-1. <https://doi.org/10.1029/2001JA000197>
- Takahashi, K., Lee, D.-H., Merkin, V. G., Lyon, J. G., & Hartinger, M. D. (2016). On the origin of the dawn-dusk asymmetry of toroidal Pc5 waves. *Journal of Geophysical Research*, 121(10), 9632–9650. <https://doi.org/10.1002/2016JA023009>
- Takahashi, K., & Ukhorskiy, A. Y. (2007). Solar wind control of Pc5 pulsation power at geosynchronous orbit. *Journal of Geophysical Research*, 112, 11205. <https://doi.org/10.1029/2007JA012483>
- Takasaki, S., Kawano, H., Tanaka, Y., Yoshikawa, A., Seto, M., Iizima, M., et al. (2006). A significant mass density increase during a large magnetic storm in October 2003 obtained by ground-based ULF observations at L ~ 1.4. *Earth Planets and Space*, 58, 617–622. <https://doi.org/10.1186/bf03351959>
- Tsyganenko, N. A., & Sitnov, M. I. (2005). Modeling the dynamics of the inner magnetosphere during strong geomagnetic storms. *Journal of Geophysical Research*, 110(A3), A03208. <https://doi.org/10.1029/2004JA010798>
- Walach, M. T., & Grocott, A. (2019). SuperDARN observations during geomagnetic storms, geomagnetically active times, and enhanced solar wind driving. *Journal of Geophysical Research*, 124(7), 5828–5847. <https://doi.org/10.1029/2019JA026816>
- Walach, M.-T., Grocott, A., & Milan, S. E. (2021). Average ionospheric electric field morphologies during geomagnetic storm phases. *Journal of Geophysical Research: Space Physics*, 126(4). <https://doi.org/10.1029/2020JA028512>
- Wang, B., Nishimura, Y., Hietala, X.-C., Shi, Q., Zhang, H., Weatherwax, A., et al. (2018). Dayside magnetospheric and ionospheric responses to a foreshock transient on 25 June 2008: 2.2-d evolution based on dayside auroral imaging. *Journal of Geophysical Research: Space Physics*, 123(0), 6347–6359. <https://doi.org/10.1029/2017JA024846>
- Wang, B., Zhang, H., Liu, Z., Liu, T., Li, X., & Angelopoulos, V. (2021). Energy modulations of magnetospheric ions induced by foreshock transient driven ultralow frequency waves. *Geophysical Research Letters*, 48(10), e93913. <https://doi.org/10.1029/2021GL093913>
- Waters, C. L., Menk, F. W., & Fraser, B. J. (1991). The resonance structure of low latitude Pc3 geomagnetic pulsations. *Geophysical Research Letters*, 18(12), 2293–2296. <https://doi.org/10.1029/91GL02550>
- Wharton, S. J., Rae, I. J., Sandhu, J. K., Walach, M. T., Wright, D. M., & Yeoman, T. A. K. (2020). The changing eigenfrequency continuum during geomagnetic storms: Implications for plasma mass dynamics and ULF wave coupling. *Journal of Geophysical Research*, 125(6), e27648. <https://doi.org/10.1029/2019JA027648>
- Wharton, S. J., Wright, D. M., Yeoman, T. K., James, M. K., & Sandhu, J. K. (2018). Cross-phase determination of ultralow frequency wave harmonic frequencies and their associated plasma mass density distributions. *Journal of Geophysical Research*, 123(8), 6231–6250. <https://doi.org/10.1029/2018JA025487>
- Wharton, S. J., Wright, D. M., Yeoman, T. K., James, M. K., & Sandhu, J. K. (2019). The variation of Resonating magnetospheric field lines with changing geomagnetic and solar wind conditions. *Journal of Geophysical Research*, 124(7), 5353–5375. <https://doi.org/10.1029/2019JA026848>
- Wharton, S. J., Wright, D. M., Yeoman, T. K., & Reimer, A. S. (2019). Identifying ULF wave eigenfrequencies in superdarn backscatter using a lomb-scargle cross-phase analysis. *Journal of Geophysical Research: Space Physics*, 124(2), 996–1012. <https://doi.org/10.1029/2018ja025859>
- Wild, J. A., Yeoman, T. K., & Waters, C. L. (2005). Revised time-of-flight calculations for high-latitude geomagnetic pulsations using a realistic magnetospheric magnetic field model. *Journal of Geophysical Research*, 110(A11), A11206. <https://doi.org/10.1029/2004JA010964>
- Wright, A. N. (1994). Dispersion and wave coupling in inhomogeneous MHD waveguides. *Journal of Geophysical Research*, 99, 159–167. <https://doi.org/10.1029/93JA02206>
- Wright, A. N., & Elsden, T. (2016). The theoretical foundation of 3D Alfvén resonances: Normal modes. *The Astrophysical Journal*, 833, 230. <https://doi.org/10.3847/1538-4357/833/2/230>
- Wright, A. N., & Elsden, T. (2020). Simulations of MHD wave propagation and coupling in a 3-D magnetosphere. *Journal of Geophysical Research*, 125(2), e27589. <https://doi.org/10.1029/2019JA027589>
- Wright, A. N., Elsden, T., & Takahashi, K. (2018). Modeling the dawn/dusk asymmetry of field line resonances. *Journal of Geophysical Research: Space Physics*, 123(0), 6443–6456. <https://doi.org/10.1029/2018JA025638>
- Wright, A. N., & Thompson, M. J. (1994). Analytical treatment of Alfvén resonances and singularities in nonuniform magnetoplasmas. *Physics of Plasmas*, 1, 691–705. <https://doi.org/10.1063/1.870815>
- Yang, B., Zong, Q.-G., Fu, S. Y., Takahashi, K., Li, X., Wang, Y. F., & Sheng, C. (2011). Pitch angle evolutions of oxygen ions driven by storm time ULF poloidal standing waves. *Journal of Geophysical Research: Space Physics*, 116(A3). <https://doi.org/10.1029/2010ja016047>
- Zong, Q., Rankin, R., & Zhou, X. (2017). The interaction of ultra-low-frequency pc3-5 waves with charged particles in Earth's magnetosphere. *Reviews of Modern Plasma Physics*, 1(1), 10. <https://doi.org/10.1007/s41614-017-0011-4>
- Zong, Q. G., Zhou, X. Z., Wang, Y. F., Li, X., Song, P., Baker, D. N., et al. (2009). Energetic electron response to ULF waves induced by interplanetary shocks in the outer radiation belt. *Journal of Geophysical Research*, 114(A10), A10204. <https://doi.org/10.1029/2009JA014393>